(ANPA Conference 2024)
ISSN: 2392-473X(Print), 2738-9537 (Online)

Research Article ©Nepal Physical Society
DOI: https://doi.org/10.3126/jnphyssoc.v10i1.72829

Spontaneous Magnetization Reversal Study of $LaMnO_3/SrTiO_3$ Thin Films

Ghadendra B. Bhandari[a)] and Mikel B. Holcomb[b)]

West Virginia University, Morgantown, West Virginia, USA.

[a)]*Corresponding author: gbb0004@mix.wvu.edu*
[b)]*Electronic mail: Mikel.Holcomb@mail.wvu.edu*

Abstract. The perovskite compound $LaMnO_3$ has gained interest due to its role as a fundamental building block in some heterostructures and its fascinating magnetic phase diagram. In bulk stoichiometric form, LMO displays A-type antiferromagnetic order. However, thin films exhibit ferromagnetic properties and spontaneous magnetization reversal for zero field cooled (ZFC) magnetization cycles. Our study examined the field-dependent variation of blocking (T_B), freezing (T_f), and compensation (T_{comp}) temperature associated with the ZFC cycle. The blocking temperature follows the relation $T_B(H) = T_B(0)(1-H/H_K)^2$, typical of magnetic nanoparticles indicating nanoclusters of spins in the thin film. The freezing and compensation temperatures exhibited exponential decay with increasing field. We examined the temperature dependence of coercivity and exchange bias. The observed trend in coercivity, combined with the absence of exchange bias, supports the presence of a mixture of weakly interacting superparamagnetic and antiferromagnetic phases. Below the blocking temperature coercivity follows the relationship $H_C(T) = H_{C0}[1-(T/T_B)^{1/2}]$.

Received: August 28, 2024; **Revised**: October 20, 2024; **Accepted**: October 31, 2024

Keywords: Magnetic thin film; magnetization reversal; blocking, freezing, and compensation temperature; Kneller's law

INTRODUCTION

The $LaMnO_3$ (LMO) exhibits a rich phase diagram due to the strong coupling between its charge, spin, and lattice degrees of freedom [1, 2]. The unique properties of LMO make it highly valuable for various applications in advanced technology memory, sensor, and data transmission technology. Ferromagnetic materials can exhibit magnetoresistive effects, which change in response to an applied magnetic field [3], and have ferromagnetic resonance under microwave and terahertz radiation [4] for data transmission. For example, the commonly fabricated ferromagnetic thin film device is the magnetic tunnel junctions (MTJs) [5]. In the development of MTJs, incorporating an additional layer of antiferromagnetic material onto the ferromagnetic reference layer can increase the coercivity of the ferromagnetic layer through the exchange bias mechanism. This enhancement in coercivity is beneficial as it broadens the detection range of the magnetic field. In some applications, the magnetic order in these layers may differ from that in the bulk material, influencing the performance and characteristics of the device.

Bulk stoichiometric LMO typically exhibits A-type antiferromagnetic (AFM) order [6]. Interestingly, when LMO is synthesized as thin films, it can display different magnetic properties compared to its bulk form. These thin films have been reported to exhibit ferromagnetic behavior [7] and even spontaneous magnetization reversal, which is quite different from the antiferromagnetic order observed in the bulk material [8, 9].

In magnetization studies, the bifurcation between field-cooled (FC) and zero-field-cooled (ZFC) curves in a magnetization vs. temperature measurement can provide significant insights into the magnetic nature of a material. This bifurcation often indicates a mixture of superparamagnetic and ferromagnetic phases within the material [10]. When these two phases coexist, the FC and ZFC curves diverge below a certain temperature, often called to as the blocking temperature. Below this temperature, the superparamagnetic particles become blocked, and their magnetization cannot easily flip, leading to a difference in the magnetization behavior when measured with and without an applied magnetic field during cooling. To understand the interaction between these different magnetic

phases, one could imagine that the superparamagnetic behavior is a diamagnetic phase that is influencing the ferromagnetic phase. For strong applied external magnetic fields, the ferromagnetic regions will dominate and align with the applied field, overcoming the opposition from the diamagnetic regions. For weak fields, the diamagnetic regions may have a more significant influence, potentially causing the ferromagnetic regions to align with the field produced by the diamagnetic regions rather than the weak external field. This complex interplay can lead to various magnetic behaviors, depending on the relative strengths of the diamagnetic and ferromagnetic regions and the applied field. In reality, the non-ferromagnetic phase is probing in exchange spring.

The observed magnetization reversal would be a result of the competition between these two magnetic interactions [8]. Magnetization reversal in certain materials can arise due to various complex magnetic interactions. For example, in RTO_3 type compounds, there is antiferromagnetic coupling between rare-earth (R: Gd, Pr, and Nd) elements and transition metals (T: Cr) may be responsible for the magnetization reversal [11]. In $YMn_{0.5}Cr_{0.5}O_3$ oxide, the competition between the Dzyaloshinsky-Moriya (DM) interaction and single-ion anisotropy can lead to magnetization reversal. To study the zero-field-cooled (ZFC) magnetization of LMO, thin films were grown on the same substrate (e.g., $SrTiO_3$ (STO) and under similar conditions, with varying thickness. The influence of temperature, magnetizing field, and thin film thickness on the magnetization is considered. Temperature dependent coercivity and exchange bias has been calculated. Magnetism is often described as a collective phenomenon arising from the behavior and distribution of spins within a material [12]. The magnetic properties observed in this study has been compared to analogous systems, particularly phenomenological fits for nanoparticles. Our thin films exhibit similar magnetic properties of nanoparticles [13].

EXPERIMENTAL

LMO thin films were grown on 5×10 mm^2 and 0.5 mm thick commercial $SrTiO_3$ (001) substrates. Substrates were baked at 1100 °C and then cleaned successively with acetone, isopropanol, and deionized water [14]. Thin films were grown in a 100% oxygen environment inside a pulsed laser deposition (PLD) chamber, maintaining an oxygen pressure of 30 mTorr. The substrates were heated in-situ to 750 °C at the rate of 15 °C/min and held at this temperature during the deposition. The $LaMnO_3$ plume was produced by bombarding the KrF excimer laser pulse (248 nm) having an energy of 300 mJ and a repetition rate of 5 Hz (fluence = 3.1 J/cm^2). After deposition, all samples were cooled down to room temperature at a rate of 15 °C/min in the same oxygen environment and pressure as during deposition.

The layer-by-layer growth of $LaMnO_3$ was monitored using an in-situ reflection high-energy electron diffraction (RHEED) [15]. The bright spots shown in Figure 1a indicate where many electrons reach the detector. The observed lines are Kikuchi line patterns formed by electron scattering. Figure 1b is diffraction after deposition. Sharp and well-defined RHEED diffraction patterns after deposition indicate a highly crystalline thin film. Figure 1c shows the RHEED patterns and oscillations during the growth of LMO films. The number of oscillations give the count for number of unit cell (uc) deposited on the substrate. The presence of RHEED oscillation and XRD peaks indicate the high quality of the thin films. As the oxygen pressure in the PLD chamber increases, the kinetic energy of the atomic and molecular species arriving at the substrate decreases, resulting in a delayed deposition rate. On average, the growth of one layer of the thin film requires 14 seconds at the pressure of 30 mTorr.

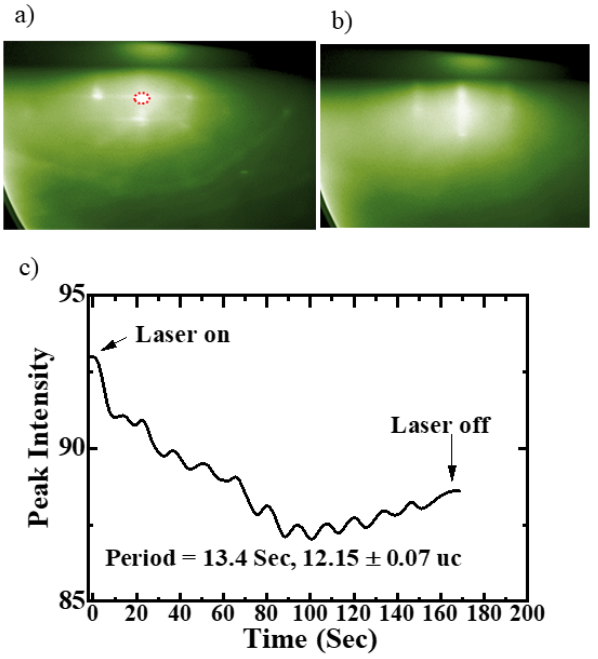

FIGURE 1. a) and b) RHEED diffraction patterns of STO substrate and 4.8 nm sample LMO/STO thin film after grown at 30 mTorr pressure, and c) RHEED intensity oscillation for the LMO film on STO, monitored at the circled point.

The c-lattice parameter was determined by x-ray diffraction. We used the Bruker D8 Discovery X-ray Diffractometer, which employs Cu K_α x-ray radiation (wavelength, $\lambda = 1.5405$ Å) as an X-ray source and 4 bounce monochromators for the high-resolution X-ray diffraction. Figure 2 shows a $(2\theta - \omega)$ XRD pattern around sub-

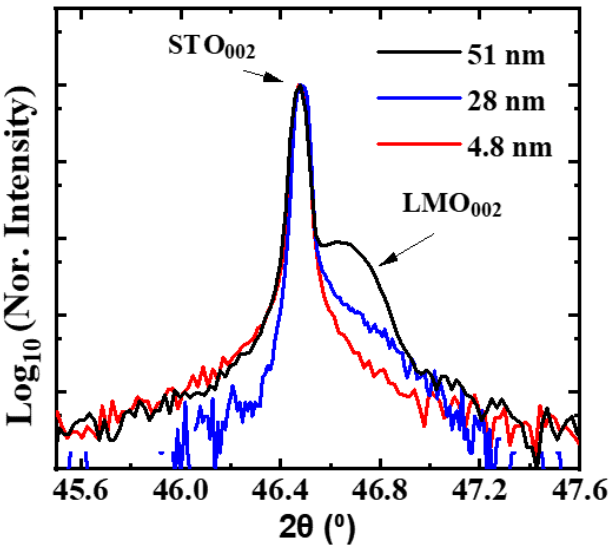

FIGURE 2. XRD of LMO (002) peak. The shoulder to the right indicates the LMO thin film.

strate's (002) diffraction peak. The bulk LMO and STO have a pseudo-cubic perovskite crystal structure with a lattice parameter of a_{LMO} = 3.88 Å and a_{STO} = 3.905 Å, respectively. The peak position of the thin film was determined by fitting a pseudo-Voigt function as described in reference [16]. The c-lattice parameter has been calculated as 3.897 ± 0.023 Å. Thicknesses were estimated by multiplying the number of unit cells from the RHEED oscillations and c-lattice parameter, as 4.8 ± 0.027 nm, 28.0 ± 0.023 nm, and 51.0 ± 0.021 nm. Samples are named according to their thickness: 4.8 nm, 28 nm, and 51 nm.

The temperature and field-dependent magnetization of the LMO samples were measured by using a vibrating sample magnetometer (VSM) with a Quantum Design physical property measurement system (PPMS-9T). The DC magnetization was measured using cycles of zero field-cooled (ZFC) and field-cooled (FC) methods. During the ZFC cycle, the sample was cooled to 5 K without any applied field and then measured while warming up in the presence of a measuring field H. In the FC cycle, the sample was cooled and measured under the applied field H. For each measurement cycle, the sample was held at 5 K for 15 minutes to ensure temperature stability. Then a measuring field (H) was applied. After finishing the measurement, the coils were demagnetized at room temperature (or at higher) to remove residuals magnetic field before cooling down the sample.

RESULTS AND DISCUSSION

The STO substrate exhibits diamagnetic properties [17], with its magnetic moment being a linear function of the applied magnetic field H, described by $M_{dia} = \chi_{Dia}H$. Assuming the magnetization of the samples is a superposition of two contributions - ferromagnetic/paramagnetic(M_{Fer}), and diamagnetic (M_{Dia}) - the total magnetization of the sample can be expressed as: $M = M_{Fer(T,H)} + \chi_{Dia}H$. For the M vs T graph, the constant negative value of M at sufficiently higher temperature than the Curie temperature; and in the case of M vs H, a negative slope at higher H indicates the diamagnetic contribution from the STO substrate. The plots of M vs T for the ZFC and FC cases measured at different H are shown in Figure 3 after subtraction of the diamagnetic contribution of the STO substrate. The measured magnetic moment is scaled to the volume of the film (thickness × area).

A bifurcation between FC and ZFC magnetization has been observed below the blocking temperature (T_B). The bifurcation represents the temperature above which all spins are unblocked [18]. Examining the FC curves, the magnetization decreases with increasing temperature, which is typical in ferromagnetic materials. Ferromagnetism is present only below a certain temperature, known as the ferromagnetic transition temperature or Curie temperature T_C. Above the Curie temperature, the material is paramagnetic, and its susceptibility is given by $M/H = \chi = C/(T - T_C)$. For 51 nm sample, T_C has been calculated as 76.21 K which is below the Néel temperature of bulk LMO. The remaining samples have also Curie temperature in the similar range of 51 nm sample. The 51 nm sample has a noticeable bump at 141 K (indicated by a vertical line in Figure 3c) which is the Néel temperature of bulk antiferromagnetic LMO. This bump is less noticeable for the 28 nm sample, and absent in the thinnest sample.

Let's look at the strength of magnetization. For instance, at 20 Oe, the maximum magnetization under FC is 45, 30, and 20 emu/cm^3 for 4.8, 28, and 51 nm samples, respectively. The maximum value of magnetization decrease with the increase in thickness of the thin film. This is correlated with the evolution of the AFM phase with the thin film thickness. Magnetization after 500 Oe slightly increases reaching to saturation. The saturation magnetization ranges from 54 -100 emu/cm^3 for the thickest to thinnest thin films. For the 28 nm sample, the saturation magnetization is 60 emu/cm^3, which is 0.35 μ_B per formula unit by considering a uniform lattice constant. This magnetic moment suggests a dilute ferromagnetic or canted antiferromagnetic property.

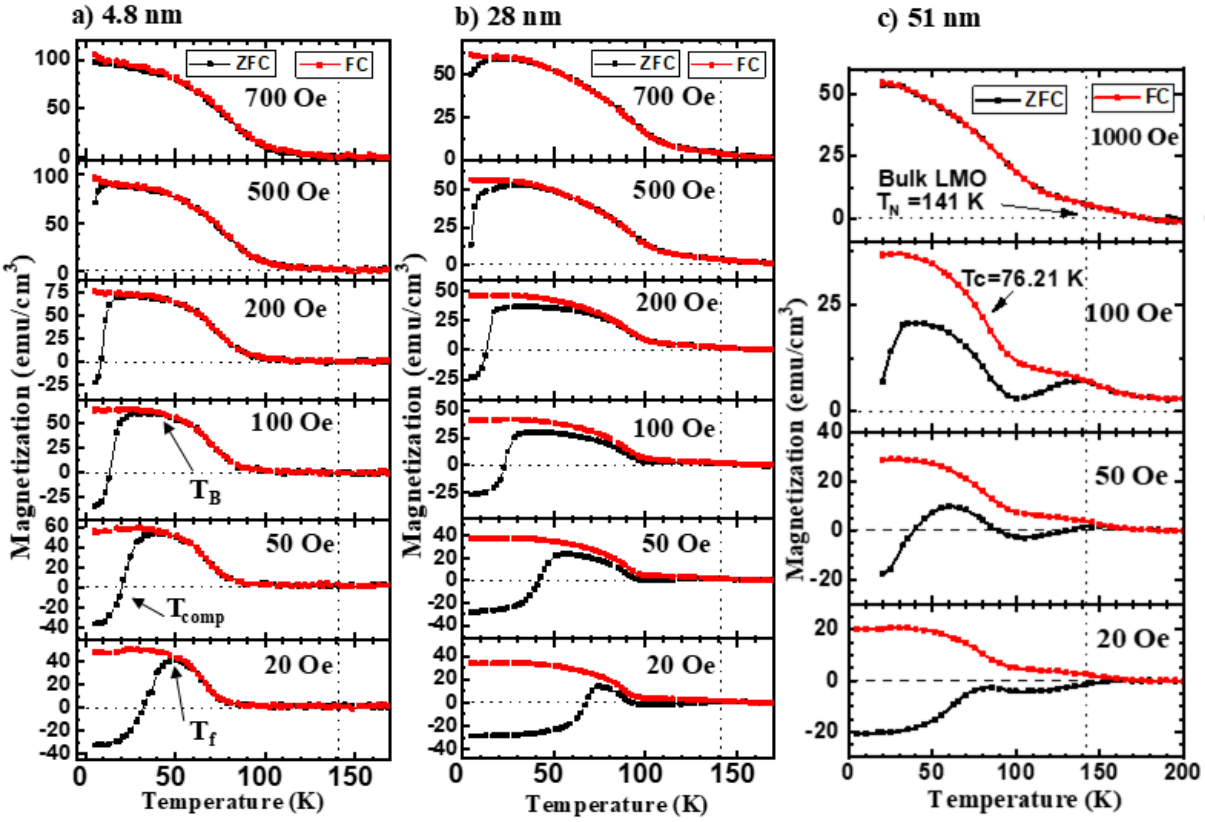

FIGURE 3. Temperature dependent magnetization M(T) curves under ZFC and FC processes with different magnetic fields for a) 4.8 nm, b) 28 nm , and c) 51 nm thick thin films. Vertical line at 141 K represents Néel temperature of bulk LMO.

1. Magnetizing field dependent blocking, freezing, and compensation temperatures

The temperature-dependent magnetization (M vs T) measurements of the samples of different thicknesses samples were conducted under magnetizing fields of H = 20, 50, 100, 200, 500, 700, and 1000 Oe in Figure 3. The ZFC negative magnetization was observed in the samples at lower measuring fields, with the effect being more pronounced in thinner samples. In particular, the 4.7 nm and 28 nm samples exhibit negative magnetization up to a field strength exceeding 200 Oe, whereas the 51 nm sample shows this behavior only at fields below 100 Oe. This indicates that thinner samples, such as the 4.7 nm and 28 nm films, exhibit stronger negative magnetization effects compared to the thicker 51 nm sample, suggesting a correlation between sample thickness and the strength of negative magnetization.

As the temperature increases, the ZFC magnetization curve $M(T)$ starts from a negative value, becomes zero at T_{comp}, and progressively rises until the freezing temperature T_f which is the maximum of the ZFC curve. Finally, it merges with the FC curve near T_B. The order of these critical temperatures is $T_{comp} < T_f < T_B$. The T_{comp}, the T_f, and the T_B are shown in Figure 3 with arrows. However, the Curie temperature T_C can be either above or below T_B. Specifically, $T_C < T_B$ for thicker samples and lower H. The variation of T_f, T_B, and T_{Comp} with respect to H is shown in Figure 4.

The decreasing trend of T_B with increasing measuring field H can be explained by Kneller's law: $T_B(H) = T_B(0)(1 - H/H_K)^2$ [19]. Here, $T_B(0)$ represents maximum blocking temperature, and H_K represents the maximum field above which blocking temperature (bifurcation) does not exist. Although $T_B(0)$ is different for 28 nm and 4.8 nm thick thin films, H_K is comparable at 1048 Oe. The presence of T_B is indicative of spin clusters. The size of spin clusters can be estimated by knowing the anisotropy constant of the film.

The shifting trends of the freezing temperature T_f and compensation temperature T_{comp} do not follow Kneller's law but instead follow an exponential decay with increasing measuring field. The $T_{comp}(H)$ data fit a single exponential decay: $T_{comp}(0) + A * exp(-(H - H_0)/\eta_1)$. The decay constant η_1 was observed to be the same for both

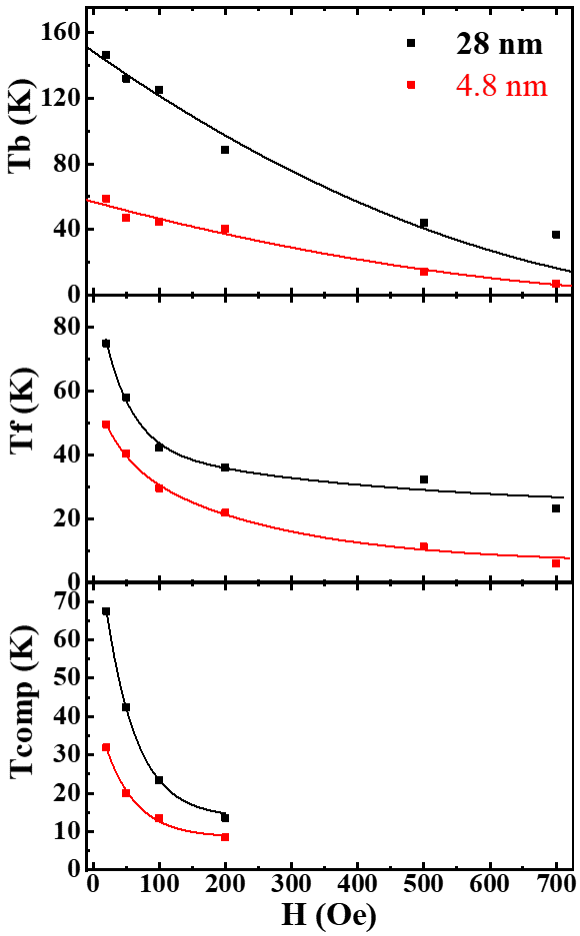

FIGURE 4. Variation of blocking temperature, freezing temperature, compensation temperature with increasing magnetic fields for 4.8 nm and 28 nm. Solid line is the fitting of the data.

samples, at 46.8 ± 1.8 Oe. In the ZFC of the 51 nm thick sample, two maxima are observed. The higher temperature maximum is associated with the AFM phase which diminishes for the 28 nm thick sample and disappears for the 4.8 nm thick sample. The lower temperature side maximum is associated with the spin freezing temperature of superparamagnetic phase. The variation of $T_f(H)$ is similar to the behavior of the freezing curve described in ref [20], and it is with a fitted double exponential decay: $T_f(H) = T_f(0) + A1 * exp(-(H - H_0)/\eta_1) + A2 * exp(-(H - H_0)/\eta_2)$. Here, η_1 for thin and thicker samples is similar (41.7 Oe) but η_2 is significantly different (402 and 238 Oe for 28 and 4.8 nm thick samples, respectively) which can indicate a thickness effect.

2. Temperature dependent hysteresis, coercivity, and exchange bias

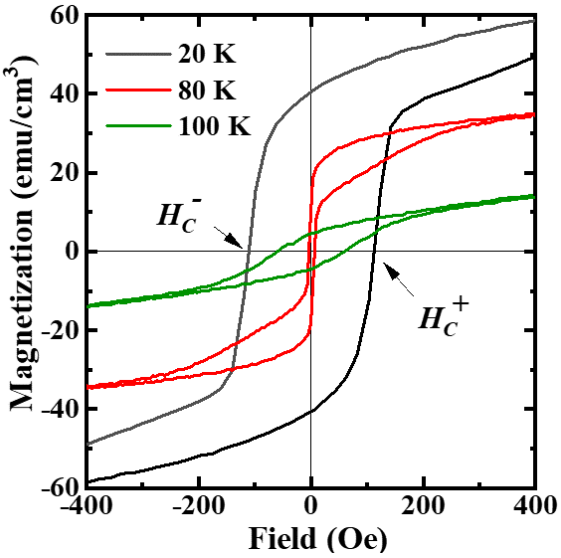

FIGURE 5. Hysteresis loops for 28 nm thick $LaMnO_3$ thin film.

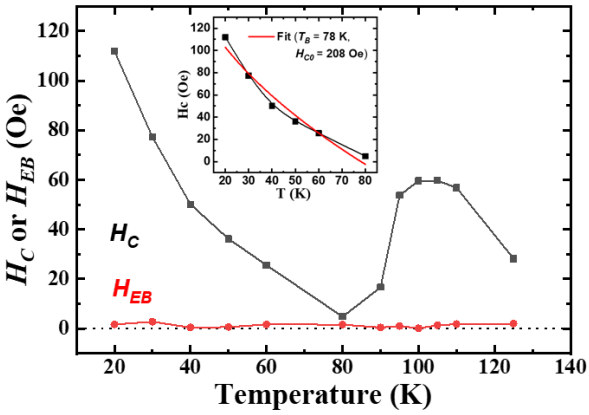

FIGURE 6. Temperature variation of coercivity (H_c) and exchange bias field (H_{EB}) for 28 nm thick $LaMnO_3$ thin film. The inset shows the fitted data.

To investigate the coercivity and the possible occurrence of the exchange bias effect, the sample is cooled down to 5 K from room temperature in the ZFC state. Hysteresis loops are recorded between 20 K to 150 K. Hysteresis taken at 20, 80, and 100 K has been plotted in Figure 5, where H_c^+ and H_c^- represent the positive and negative coercive fields, respectively. The coercive field (H_c) and exchange bias (H_{EB}) have been estimated

as $|\frac{H_C^+ - H_C^-}{2}|$ and $|\frac{H_C^+ + H_C^-}{2}|$, respectively. The temperature variation of the exchange bias field (H_{EB}) and the coercive field (H_c) is shown in Figure 6. H_c is large at the lower temperatures region, decreases with increasing temperature and reaches to minimum at 80 K which is near the Curie temperature. It then increases rapidly, reaching a maximum near 100 K before decreasing again. This trend of H_c is similar to that observed in NiO powder samples and in Monte Carlo simulations of antiferromagnetic nanoparticles [21], where the coercivity is minimal for small nanoparticles and maximized for large single domain nanoparticles [22]. Equivalently, the distribution of spins is in nanoclusters in the case of thin films. Additionally, composites of ferromagnetic (FM) and antiferromagnetic (AFM) exhibit exchange bias due to interfacial interaction between FM and AFM particles or thin films. This exchange interaction is evidenced by a shift of the hysteresis loops along the field axis below the ordering temperature of the AFM phase [23]. No shift of the hysteresis loops has been observed. The absence of exchange bias is correlated with the very small particle size [21].

For randomly oriented and non-interacting nanoparticles, the temperature-dependent coercive field for temperature range $0 - T_B$ varies as $H_C(T) = H_{C0}[1 - (T/T_B)^{1/2}]$ [24]. Here, T_B represents the superparamagnetic blocking temperature of the nanoparticles. H_{C0} represents the coercivity at $T = 0$ K. This equation has been fitted for the temperature range 20 - 80 K. The fitted blocking temperature T_B is 78 $\pm$ 4 K, which is close to the actual blocking temperature obtained from M vs T with an applied magnetizing field of 200 Oe.

3. Field dependent magnetization.

In addition to the minimum coercivity measured for the 28 nm thick sample, the $M(H)$ loop has some extra features which have been indicated by an arrow in Figure 7 for the hysteresis measured at 80K. This suggests the presence of coercivity from another phase, which can be separated by fitting the following function [25].

$$M(H) = A1 \arctan\frac{H \pm H_{C1}}{w1} + A2 \arctan\frac{H \pm H_{C2}}{w2}$$

where A_i are the amplitudes of the component loops, H_{Ci} are the coercivities, w_i are the broadenings. Here, the index 1 denotes the soft (low coercivity) loop, while 2 denotes the hard (large coercivity) component. The fit to the hysteresis data is shown in Figure 7, revealing a good fit to the model. From the fit, H_{C1}= 2.5 Oe and $A1$ = 11 emu/cc for the 1st phase, while H_{C2}= 56 Oe and $A2$ = 16 emu/cc for the second phase were extracted.

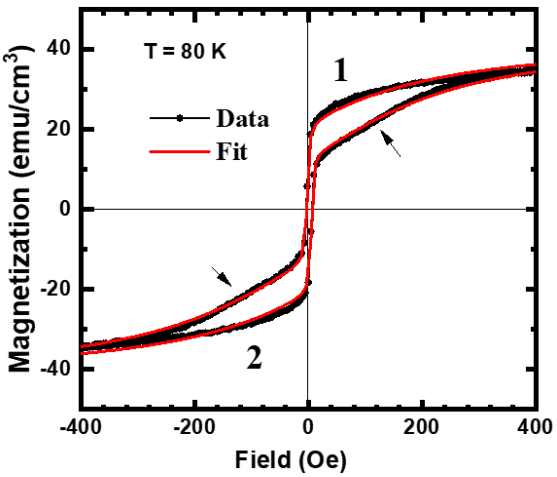

FIGURE 7. Fitting of hysteresis loops. Loops 1 and 2 are for decreasing and increasing magnetizing fields.

CONCLUSION

In this study, we investigated the magnetic properties of $LaMnO_3$ thin films, revealing the presence of two distinct magnetic phases. The distribution of spins has been studied by some phenomenological fitting and comparing with similar systems. The separation of magnetization for the FC and ZFC data suggests the two distinct magnetic phases including superparamagnetic phase. Ferromagnetic nanoclusters of spins is playing the role of superparamangetic phase. From the FC cycle, magnetic moment per formula unit has been estimated as 0.35 μ_B which indicates a dilute ferromagnetic property. The blocking temperature's dependence on the applied magnetic field follows a relation typical of magnetic nanoparticles, indicating the formation of nanoclusters in the thin film. The freezing and compensation temperatures exhibit exponential decay with increasing field. The observation of trend of temperature dependent coercivity and no exchange bias indicate that the thin films have a mixture of weakly interacting superparamagnetic and antiferromagnetic phases. The antiferromangetic ordering of spins in $LaMnO_3$ cannot be overlooked. Ultimately, our thin film exhibits magnetic properties similar to a mixture of superparamagnetic and antiferromagnetic nanoparticles. The spontaneous magnetization reversal observed in the ZFC magnetization cycle is likely associated with superparamagnetic nanoclusters that are weakly pinned to the antiferromagnetic phase. This comprehensive study of the fascinating magnetic properties-magnetization reversal in $LaMnO_3$ during ZFC provides valuable insights for further exploration of its applications in magnetic heterostructure devices.

ACKNOWLEDGEMENTS

This work is partially supported by NASA EPSCoR Award # 80NSSC22M0173.

EDITORS' NOTE

This manuscript was rigorously peer-reviewed and subsequently accepted for inclusion in the special issue of the Journal of Nepal Physical Society (JNPS) after it was submitted to the Association of Nepali Physicists in America (ANPA) Conference 2024.

REFERENCES

1. Y. Liu, H. F. Wong, K. Lam, C.-L. Mak, and C. W. Leung, "Tuning ferromagnetic properties of $LaMnO_3$ films by oxygen vacancies and strain," Journal of Magnetism and Magnetic Materials **481**, 85–92 (2019).
2. M. S. Tumusange, G. B. Bhandari, Z. Romestan, P. Uprety, I. P. Subedi, A. H. Romero, M. B. Holcomb, and N. J. Podraza, "Interpretation of complex optical properties and optical transitions of epitaxial lamno3 thin films," Applied Surface Science , 160682 (2024).
3. X. Liang, C. Dong, H. Chen, J. Wang, Y. Wei, M. Zaeimbashi, Y. He, A. D. Matyushov, C. Sun, and N. X. Sun, "A review of thin-film magnetoelastic materials for magnetoelectric applications," Sensors (Basel, Switzerland) **20** (2020).
4. A. V. Bogomolova, S. A. Nikitov, F. Yu. Ogrin, and S. V. Grishin, "Magnetic bias field driven ferro- and antiferromagnetic semiconductors as double negative media for microwave and terahertz ranges," Journal of Magnetism and Magnetic Materials **587**, 171278 (2023).
5. C. Yufeng, G. Wang, S. Zhengfeng, W. Sheng-gao, M. Yangwu, D. Quanrong, and Y. Jingjing, "Magnetic characteristics of $LaMnO_{3+\delta}$ thin films deposited by rf magnetron sputtering in an O_2/Ar mixture gas," Materials Research Express **8** (2021), 10.1088/2053-1591/abd6a3.
6. G. Matsumoto, "Study of $(La_{1-x}Ca_x)MnO_3$. i. magnetic structure of $LaMnO_3$," Journal of the Physical Society of Japan **29**, 606–615 (1970).
7. M. Li, C. Tang, T. R. Paudel, D. Song, W. Lü, K. Han, Z. Huang, S. Zeng, X. Renshaw Wang, P. Yang, Ariando, J. Chen, T. Venkatesan, E. Y. Tsymbal, C. Li, and S. J. Pennycook, "Controlling the magnetic properties of lamno3/srtio3 heterostructures by stoichiometry and electronic reconstruction: Atomic-scale evidence," Advanced Materials **31**, 1901386 (2019), https://onlinelibrary.wiley.com/doi/pdf/10.1002/adma.201901386.
8. M. B. Holcomb, G. B. Bhandari, and N. Mottaghi, "Investigating magnetism for spintronics," in *NanoScience + Engineering* (2023).
9. A. A. de Faria Jr, M. B. Holcomb, and G. B. Bhandari, "Modified heisenberg model of spin clusters to relate to the spontaneous magnetization reversal," in *Spintronics XVII*, Vol. 13119 (SPIE, 2024) pp. 147–156.
10. J. Yang, J. Kim, J. Lee, S. Woo, J. Kwak, J. Hong, and M. Jung, "Inverted hysteresis loops observed in a randomly distributed cobalt nanoparticle system," Phys. Rev. B **78**, 094415 (2008).
11. L. D. Tung, M. R. Lees, G. Balakrishnan, and D. McK. Paul, "Magnetization reversal in orthovanadate rVo_3 compounds (r = La, Nd, Sm, Gd, Er, and Y): Inhomogeneities caused by defects in the orbital sector of quasi-one-dimensional orbital systems," Phys. Rev. B **75**, 104404 (2007).
12. P. Papon, J. Leblond, and P. H. E. Meijer, *The physics of phase transitions* (Springer, Berlin, Heidelberg, Berlin, Heidelberg, 2001) pp. 211–245.
13. N. Mottaghi, M. S. Seehra, R. Trappen, S. Kumari, C.-Y. Huang, S. Yousefi, G. B. Cabrera, A. H. Romero, and M. B. Holcomb, "Insights into the magnetic dead layer in La0.7Sr0.3MnO3 thin films from temperature, magnetic field and thickness dependence of their magnetization," AIP Advances **8**, 056319 (2018), https://pubs.aip.org/aip/adv/article-pdf/doi/10.1063/1.5005913/12980766/056319_1_online.pdf.
14. R. Bachelet, F. Sanchez, J. Santiso, C. Munuera, C. Ocal, and J. Fontcuberta, "Self-assembly of srtio3(001) chemical-terminations: A route for oxide-nanostructure fabrication by selective growth," Chemistry of Materials **21**, 2494–2498 (2009).
15. T. Ohnishi, H. Koinuma, and M. Lippmaa, "Pulsed laser deposition of oxide thin films," Applied Surface Science **252**, 2466–2471 (2006), proceedings of the Third Japan-US Workshop on Combinatorial Material Science and Technology.
16. C. Suryanarayana and M. G. Norton, *X-Ray diffraction : a practical approach* (Springer US, Boston, MA, 1998).
17. H. P. R. Frederikse and G. A. Candela, "Magnetic susceptibility of insulating and semiconducting strontium titanate," Phys. Rev. **147**, 583–584 (1966).
18. K. Pisane, E. Despeaux, and M. Seehra, "Magnetic relaxation and correlating effective magnetic moment with particle size distribution in maghemite nanoparticles," Journal of Magnetism and Magnetic Mterials **384**, 148–154 (2015).
19. V. Singh, M. S. Seehra, and J. Bonevich, "Nickel-silica nanocomposite: Variation of the blocking temperature with magnetic field and measuring frequency," Journal of Applied Physics **103**, 07D524 (2008), https://pubs.aip.org/aip/jap/article-pdf/doi/10.1063/1.2834246/13356993/07d524_1_online.pdf.
20. S. Lin, D. F. Shao, J. C. Lin, L. Zu, X. C. Kan, B. S. Wang, Y. N. Huang, W. H. Song, W. J. Lu, P. Tong, and Y. P. Sun, "Spin-glass behavior and zero-field-cooled exchange bias in a cr-based antiperovskite compound pdncr3," J. Mater. Chem. C **3**, 5683–5696 (2015).
21. E. Winkler, R. D. Zysler, D. Vasquez Mansilla, D. Fiorani, D. Rinaldi, D. Vasilakaki, and K. N. Trohidou, "Surface spin-glass freezing in interacting core–shell nio nanoparticles," Nanotechnology **19**, 185702 (2008).
22. J. Sung Lee, J. Myung Cha, H. Young Yoon, J.-K. Lee, and Y. Keun Kim, "Magnetic multi-granule nanoclusters: A model system that exhibits universal size effect of magnetic coercivity," Scientific Reports **5**, 12135 (2015).
23. P. Dobrynin, A. N.and Warin, A. Vorobiev, and D. Givord, "On the origin of positive exchange bias and coercivity enhancement in proximity to the blocking temperature," Journal of Magnetism and Magnetic Materials **520**, 166707 (2021), magnetic materials and their applications: in Memory of Dominique Givord.
24. F. C. Fonseca, G. F. Goya, R. F. Jardim, R. Muccillo, N. L. V. Carreño, E. Longo, and E. R. Leite, "Superparamagnetism and magnetic properties of ni nanoparticles embedded in sio_2," Phys. Rev. B **66**, 104406 (2002).
25. R. Trappen, A. J. Grutter, C.-Y. Huang, A. N. Penn, N. Mottaghi, S. Yousefi, A. Haertter, S. Kumari, J. M. Lebeau, B. J. Kirby, and M. B. Holcomb, "Effect of oxygen stoichiometry on the magnetization profiles and negative magnetization in lsmo thin films," Journal of Applied Physics (2019).